Cavities for light and sound: a cavity-enhanced platform for quantum acoustics

Fisicaro, M.

5 Active stabilization of an open-access optical microcavity for low-noise operation in a standard closed-cycle cryostat

Open-access optical microcavities are Fabry-Perot type cavities consisting of two micrometer-size mirrors, separated by an air (or vacuum) gap typically of a few micrometers. Compared to integrated microcavities, this configuration is more flexible as the relative position of the two mirrors can be tuned, allowing for easy changes in parameters such as cavity length and mode volume and the selection of specific transverse cavity modes. These advantages come at the expense of the mechanical stability of the cavity itself, which is particularly relevant in noisy closed-cycle cryostats. Here, we show an open-access optical microcavity based on scanning-probe microscope design principles. When operated at 4 K in a tabletop optical closed-cycle cryostat without any dedicated mechanical low-pass filter, we obtain stabilities of 5.7 and 10.6 pm rms in the quiet and full periods of the cryocooler cycle, respectively. Our device has free-space optical access, essential, for instance, for full polarization control.

This chapter is based on: M. Fisicaro, M. Witlox, H. van der Meer, and W. Löffler, Active Stabilization of an Open-Access Optical Microcavity for Low-Noise Operation in a Standard Closed-Cycle Cryostat, Review of Scientific Instruments 95, 033101 (2024) [60].

5.1 Introduction

Optical microcavities are a powerful tool to enhance the interaction between light and quantum systems [127]. Depending on the strength of this interaction, it enables different applications: in the weak coupling regime, the Purcell effect enables highly efficient extraction of photons for single photon sources as well as counteracting dephasing by the increased spontaneous emission rate in the desired optical mode [53–56, 128], while the strong coupling regime enables deterministic interaction between distant quantum emitters and two-photon quantum gates [129–134]. Open-access microcavities are a miniaturized version of Fabry-Perot optical cavities, consisting of two mirrors where at least one has a micrometer-scale curvature and which can be positioned with very high precision with respect to each other [135, 136]. While maintaining a small mode volume and potentially high finesse [58, 137, 138], they allow tuning of the resonance frequency and transverse cavity mode [139], spatial positioning of the cavity mode with respect to quantum emitters, and a high coupling or collection efficiency [56, 136, 140].

For the above-mentioned applications, many quantum emitters require cooling down to a few Kelvin, ideally around 4 K for self-assembled semiconductor quantum dots, and the cavity needs to be mechanically stable to maintain spectral overlap with an optical transition of the quantum emitter. While helium bath cryostats can be made mechanically very quiet, resulting in a very high mechanical stability of the cavity with root mean square (rms) fluctuations of the cavity length down to 4.3 pm [58,138], it would be highly advantageous to be able to use instead a tabletop optical closed-cycle cryostat without the need for liquid helium, enabling portability and minimizing maintenance.

Because of the noisy nature of closed-cycle cryostats, the realization of stable open-access microcavities is challenging. Recent developments have been made with fiber-based microcavities by using mechanical low-pass filters in the cryostat [59,141–143], and fluctuations of the cavity length as low as 15 pm rms have been obtained in noncontact mode, down to 0.8 pm rms when the cavity is operated with direct contact between the two mirrors [59]. However the use of a mechanical low-pass filter is not trivial in combination with free-space optical coupling to the cavity. A low-pass filter is essentially a low-Q harmonic oscillator [144], and while it rejects high-frequency vibrations, it introduces inevitably a time dependent sideways motion of the whole open-cavity device with respect to the laser beam. This sideways motion happens at the resonance frequency of the low-pass filter and can cause time dependent fluctuations in the optical power coupled to the cavity.

Here, we show that for an open microcavity with free-space optical access, it is possible to achieve high stability in an optical tabletop closed-cycle cryostat (Montana Cryostation s100 with Gifford-McMahon cryocooler) without using a dedicated mechanical low-pass filter, by careful mechanical design of the open-cavity device and using conventional feedback stabilization. In particular, without direct contact between the two mirrors, we demonstrate sub-picometer stability at room temperature, while in a tabletop closed-cycle cryostat at 4 K, we reach stabilities of 5.7 and 10.6 pm rms in the quiet and full periods of the cryocooler, respectively.

5.2 Device design

Our open microcavity has a plano-concave configuration, where we use a large flat bottom thin-film mirror and, as the top concave mirror, a commercial chip containing an array of

micro-mirrors with radii of curvature ranging from 10 to 100 µm. The desired top mirror can be selected by adjusting the external mode-matching optics. The two mirrors need to be kept at a fixed distance by a device that allows for nanometric alignment of the two mirrors with respect to each other along the three spatial directions and two angles, while being insensitive to vibrations in order to operate in a mechanically noisy environment. This is because the cryo-cooler used in closed-cycle cryostats produces periodic mechanical pulses that propagate through the cryostat, reaching the open-cavity device and exciting its mechanical resonances. As a result, the distance between the two mirrors is subject to fluctuations induced by these vibrations.

The consequences of these vibrations are more or less severe depending on the cavity finesse which is determined by the mirror reflectivity. In order to maintain resonance of the laser with respect to the cavity (or quantum emitters therein), the fluctuations of the cavity length must be much smaller than the FWHM (full width at half maximum) of the cavity resonance. In our case, we aim to use the cavity for a Purcell-enhanced quantum-dot single photon source, and therefore, a modest finesse is sufficient [53–56]. The coating of the concave micromirrors was, therefore, designed for a cavity with a finesse of F ~ 2500 at a wavelength of $\lambda = 935$ nm, which results in a FWHM of the cavity resonance in terms of cavity length change of $\Delta L_{FWHM} \sim 190$ pm, where ΔL_{FWHM} is given by

$$\Delta L_{FWHM} = \frac{\lambda}{2F}. \tag{5.1}$$

The fluctuations in the cavity length must be much smaller than this value. For example, for fluctuations 10 times smaller than ΔL_{FWHM}, we require a stability of 19 pm.

This is extremely challenging, and because fully tunable open access optical microcavities are relatively new, most of the techniques and approaches related to the design of such systems are not very well established in the field of optics. However, the same challenges can be found in scanning probe microscopes (SPMs) that have been developed since the 1980s, where the challenge is to keep the tip-sample distance stable in the same way as for the two mirrors here. For SPMs, ultra-high mechanical stabilities have been achieved in a closed cycle cryostat, with a tip-sample distance variation up to 1.5 pm [145] but only if a helium exchange gas vibration isolation system is used, and even a higher stability in a He bath cryostat, with an average vibration level of ~6 fm/$\sqrt{\text{Hz}}$ [146]. With this in mind we decided to design our device shown in Fig. 5.1 following the principles and guidelines adopted in the design of scanning tunneling microscopes (STMs) [144, 146].

As shown in Figs. 5.1(a) and 5.1(b), the device is divided into two parts: the top plate and the bottom part. The bottom flat mirror (1) is mounted with grease on a custom-built high-stiffness XY translation stage (2) that consists of a polished sapphire plate on top of a XY shear piezo glued to the bottom part of the device, similar to those used in STMs [147]. The XY stage has a step size in the nanometer range with a travel range of about 5 mm. The top plate has a hole in its center for optical access.

On the bottom side of the top plate, the top cavity mirror mount is attached in an assembly that consists of a ring-shaped alumina disk (3), a ring piezo (4), another alumina ring-shaped disk (5), and the micro-mirrors array (6), all glued together with epoxy adhesive (EPO-TEK H74F), which is proven to enable strong and stiff connections in SPM vacuum applications. The thickness of the alumina disks has been chosen to minimize cavity length changes during cooldown.

The ring piezo (4) (Noliac NAC2125) is used for precision scanning and active stabilization of the cavity length. The relative alignment of the two cavity mirrors is accomplished

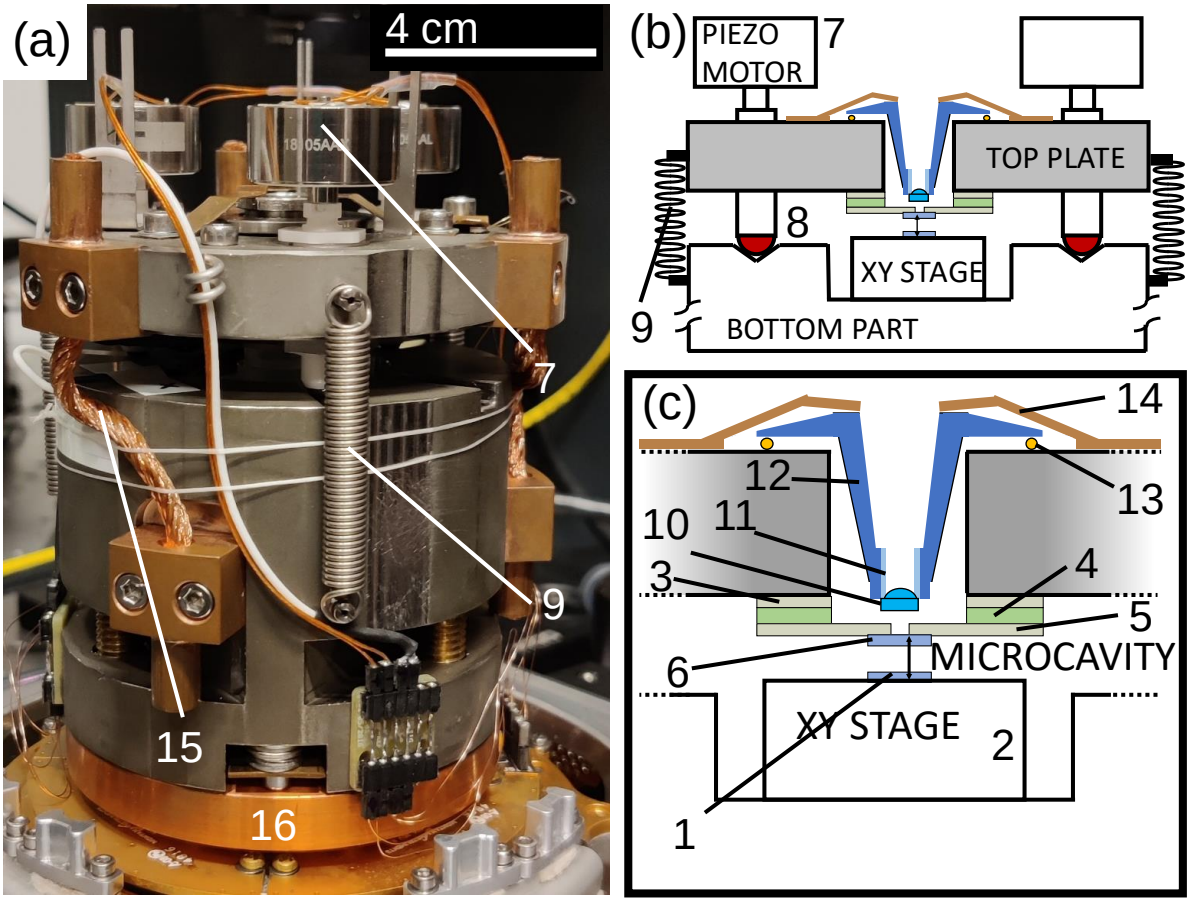

Figure 5.1: Picture of the open-cavity device (a) and corresponding not-to-scale sketches (b), and (c). The top plate and bottom part, as well as the lens mount (11, 12), are made from invar and held together by springs; the bottom part is clamped to the cold base plate of the cryostat by a copper adapter disk (16). Three copper braids are used to cool the top plate (15). The other elements are described in the main text.

with three piezo motors (JPE CLA 2201) in a tip-tilt configuration (7), which enables adjustment of the distance as well as the angles between the top and bottom mirrors with nanometric precision.

To ensure mechanical stability and to decouple the movement of the top plate from a XY translation, the three ceramic spherical tips (8) at the end of the spindle of the piezo motors rest on three v-grooves engraved on the upper side of the bottom part. Finally, the top plate and bottom part are held together with three metal springs (9) each exerting a force of 12 N, tuned such that the piezo motors operate well. Mode matching to the microcavity mode is achieved with an aspheric lens with 0.4 NA (10), mounted in a lens holder consisting of an invar micrometric screw (11) in a threaded invar cone (12) housed in the central hole of the top plate.

The lens holder has a smaller diameter than the hole in the top part, in such a way that the lens can be translated in the XY plane for alignment with the optical microcavity mode, and rests on three ruby balls (13) of 1 mm diameter, glued into holes made in the top invar plate. After aligning the lens in the XY plane and along the z direction (with the micrometric inner screw), it is clamped down with three leaf springs (14). To achieve cooling of the top plate, we thermally connected it to the bottom part of the open-cavity

device using three copper braids (15). This soft connection minimizes the amount of vibration transferred to the top plate. The bottom part is clamped to the cold base plate of the cryostat by a copper adapter disk (16), without a dedicated mechanical low-pass filter between the cryostat and our device.

The choice of the particular ring piezo mounted on the top plate is a compromise, as usually one would choose a small-diameter piezo element with small capacitance and, therefore, high bandwidth, but our choice is limited by the mode matching lens. Due to its short working distance (3.39 mm), in order to get close to the concave top cavity mirror, the lens must fit in the hole of the ring piezo, therefore limiting its minimum size. The material of choice for the bottom part, top plate, and lens mount is Invar-36, which has been proven to be a good solution in designing optical cryogenic systems due to its low thermal expansion coefficient [148], which ensures minimal optical realignment after cool-down.

The use of nanopositioners and piezo elements is crucial for the alignment and operation of the microcavity, but the complex structure of these actuators introduces mechanical resonance frequencies into the device. In particular, the lowest-frequency mechanical resonance of the cavity device that significantly affects the cavity length reduces the passive mechanical stability [144] and the maximum possible bandwidth of the feedback stabilization circuit [149]. In order to push this mechanical resonance as high as possible in frequency, we maximized the stiffness of the open-cavity device by connecting the different parts together by using either springs with high spring constants or a high-performance epoxy adhesive. In addition, we preserved, as much as possible, a rotational symmetry with respect to the central axis of the open-cavity device; this avoids mechanical mode-splitting and reduces the number of mechanical resonances in the device.

5.3 Device characterization: feedback loop and mechanical resonances

We now introduce the experimental setup that we will use in the rest of this paper. We discuss the negative feedback circuit used for active stabilization of the cavity length, and we show how, by measuring the transfer function of this feedback loop, we can characterize the resonances of the open-cavity device [150–152]. This knowledge is of extreme importance not only because the lowest mechanical resonance can pose a serious limitation on active stabilization, but also because it limits the passive stability, as discussed in Ref. [144]. The identification of the mechanical resonances helped us improve the stability of the open-cavity device by redesigning some of its parts iteratively.

5.3.1 Optical setup:

We operate the microcavity in reflection, as shown in Fig. 5.2: a collimated laser beam is sent to the mode-matching lens of the open-cavity device, which couples light to the cavity; the reflected light travels back along the same path and is redirected to a photodiode (Thorlabs PDA-36 EC) by a beam splitter. Before reaching the photodiode, part of the light is also sent to an imaging CCD by a pellicle beam splitter, allowing imaging of the micro-mirrors array and observation of the shape of the particular transverse mode excited in the cavity.

We use narrow-linewidth tunable diode lasers in a range from $\lambda = 935$ nm to 1000 nm.

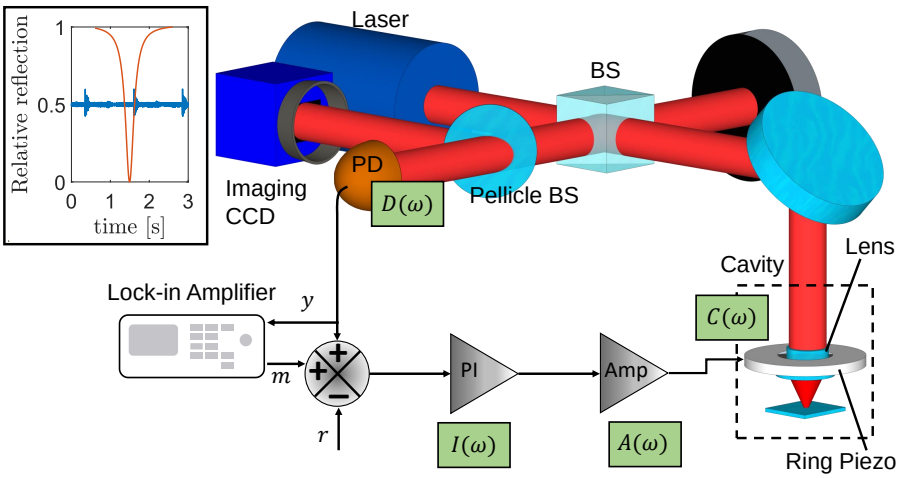

Figure 5.2: Optical scheme for measuring the open-loop transfer function of the feedback loop: laser light is coupled to the cavity, and the backreflection is both monitored with an imaging CCD and measured by a photodiode, giving a signal y. The difference between y and the (constant) reference signal r is the error signal that is fed into the proportional-integral (PI) controller that controls the ring piezo via an amplifier. A lock-in amplifier is used to measure the signal y from the photodiode and to add a modulation m on top of it in order to measure the open loop transfer function of the feedback system. The inset shows the cavity reflection dip as well as a time trace of the stabilized cavity length.

The thin-film coating of our cavity micro-mirrors is centered at $\lambda = 935$ nm, for which the cavity has a finesse F of ~ 2500. The maximum coupling efficiency we obtained at $\lambda = 935$ nm is $\eta = 64\%$, and we reach $\eta = 80\%$ at a different wavelength where the cavity has a finesse $F = 500$. We have identified the scattering losses of the mirrors as the main limiting factor for the coupling efficiency. The cavity resonance reflection dip is shown in the inset of Fig. 5.2.

5.3.2 Cavity stabilization feedback loop

In order to keep the cavity resonant with the laser, we use active stabilization of the cavity length. The signal from the photodiode is first sent through a lockbox (PI controller with scanning and locking capabilities), and then through a low noise piezo amplifier (Falco Systems WMA-200) that drives the ring piezo. Each of these stages has a specific frequency-dependent complex transfer function, defined as the ratio between the output and input voltages of that stage. Here and in the following, we will use interchangeably the words "gain" and "transfer function". We define the transfer functions of the PI controller as $I(\omega)$, the piezo amplifier $A(\omega)$, the optical microcavity $C(\omega)$, and the photodiode $D(\omega)$. The product of these quantities, $G(\omega) = IACD$, is the open loop gain of the feedback loop, i.e., the ratio between the voltage measured on the photodiode and the voltage entering the PI controller, when the output of the photodiode is disconnected from the PI controller, i.e., when the feedback loop is open.

We now quantify the contribution of each individual stage in order to provide insight into the overall gain G. I is the gain of the PI controller, and it is given by $I(\omega) = 1/(j\omega\tau_I) + G_P$, where the frequency dependent part is given by the integrator and the

constant part is given by the proportional term. τ_I is the integration time, which is inversely proportional to the integral gain. The piezo amplifier has a gain $A(\omega) = A_0/(1+ j\omega/\omega_c)$, where $\omega_c = 2\pi f_C$. In our case, $A_0 = 20$, and the cutoff frequency is $f_c = 4600$ Hz when the amplifier is driving the ring piezo, which has a capacitance of 700 nF. The gain of the cavity $C(\omega)$ and the photodiode $D(\omega)$ are a bit more complicated, as they involve a conversion from the input voltage to different physical quantities.

First, the input voltage to the piezo results in a displacement based on the piezoelectric coefficient r_{piezo} [nm/V], then this displacement changes the cavity length, which in turn changes the amount of light power that is reflected back and sent to the photodiode, as shown in the inset of Fig. 5.2. This power is then converted into a voltage signal by the photodiode. Since we will lock the cavity at half of the reflection dip (side-of-fringe lock), which gives maximum sensitivity to changes in the cavity length, we determine the combined gain of the cavity and photodiode: $CD(\omega) = -r_{piezo} \times 2\eta V_0 F/\lambda$, where η is the coupling efficiency of the light to the cavity, F is the finesse, λ is the wavelength of the incident light, and V_0 is the voltage on the photodiode when the cavity is tuned off-resonance. This gain is different for different measurements since we vary the cavity finesse by adjusting the laser wavelength, which also changes the laser power and, consequently, V_0. Moreover, the piezoelectric coefficient is $r_{piezo} = 3.8$ nm/V at room temperature but becomes a factor ~ 3 lower when operating the cavity at 4 K. As an example, at room temperature we have $CD = 7.1$ for $\lambda =$ 935 nm, $F = 2500$, and a typical value of $V_0 = 0.7$ V and $\eta =$ 0.5.

5.3.3 Identification of mechanical resonances

In reality, however, CD is not constant, and its frequency dependency can be used to find the mechanical resonances of the open cavity device. The ring piezo is mechanically coupled to the rest of the open cavity device and, therefore, to all its mechanical resonances.

Because of this, the piezoelectric coefficient r_{piezo} is, in fact, frequency dependent and will show a resonance–anti-resonance behavior in proximity to the mechanical resonances present in the system [153]. This shows up in the total open loop transfer function of the feedback loop, as shown in Fig. 5.3. This measurement has been done with a locked cavity, using a lock-in amplifier to apply a frequency-swept small modulation m to the input port of the PI controller and to measure the signal from the photodiode y, from which the open-loop gain G is calculated as

$$G(\omega) = \frac{H(\omega)}{1 + H(\omega)}, \text{ with } H(\omega) = \frac{y(\omega)}{m} \ . \tag{5.2}$$

By performing several measurements of the transfer function G while damping, removing, or changing the configuration of specific parts of the open-cavity device, we were able to identify the origin of several mechanical resonances and redesign the responsible components in order to remove or shift them to higher frequencies. After device optimization, we obtain the transfer function G shown in Fig. 5.3 of the device mounted in the cryostat at room temperature (red curve) and 4 K with the cryocooler on (blue curve).

The cryocooler leads to noise, particularly visible at low frequencies. We observe only a small shift and change in the resonance frequencies while cooling down. At 4 K, the first -π phase crossing happens at 4.1 kHz, and the first unity gain frequency is at 8.58 kHz, while the feedback loop oscillation frequency is 22.8 kHz. For a simple system with

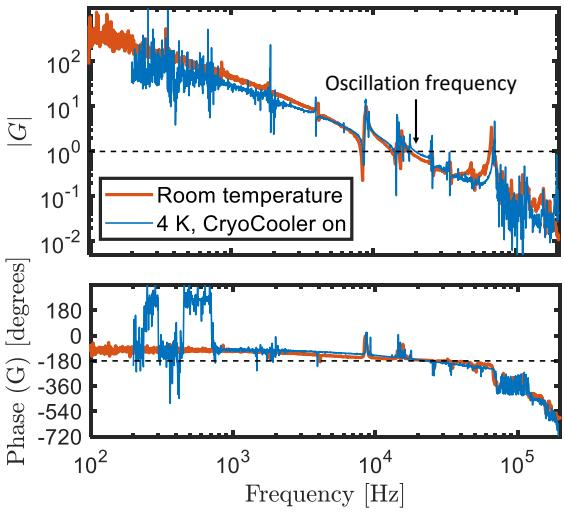

Figure 5.3: Measured amplitude and phase (unwrapped) of the feedback loop transfer function for two different conditions: device mounted in the cryostat with the cryocooler switched off at room temperature and ambient pressure (red), and at 4 K with the cryocooler on (blue). The positions of the mechanical resonances are not significantly shifted at low temperatures. The dashed lines correspond to unity gain and -π phase, respectively; the feedback loop oscillates at 22.8 kHz if the gain is set too high.

only one mechanical resonance, these three frequencies would coincide, but our open-cavity device is more complex as there are many mechanical resonances coupled with the resonance of the ring piezo. We identified some of the resonances to be drum modes of the top plate (8.58, 14.3, 15.6, 26 and 35 kHz) but we were not able to pinpoint the origin of the resonances at 1.8, 2 and 4.1 kHz.

5.4 Stability at room temperature

To measure the stability of the cavity, we use the scheme shown in Fig. 5.2 but without the modulation signal m, and again lock the cavity to the laser frequency using a side-of-fringe lock. In particular, we lock the cavity at half the depth of the reflection dip, and we record ten time traces of 10 s of the photodiode signal at a sample rate of 200 kHz. After a proper calibration (see Appendix 5.7.2) we calculate the power spectral density (PSD) of these time traces, corresponding to fluctuations in the cavity length. In Fig. 5.4 we show data measured (i) on the optical table resting on air dampers, (ii) in the cryostat under vacuum, (iii) in the cryostat under vacuum with the cryocooler switched on but still at room temperature, and (iv) in the same conditions as (iii) but only considering the quiet periods of the cryocooler, corresponding to 40% of the full period. Panel (a) shows a section of the time traces, and (b) shows the corresponding PSDs. The finesse of the cavity is 1500, and the PI parameters are $\tau_I = 30\ \mu s$, $G_P = 0.17$.

Comparing the measurements without a cryocooler, it is clear that the cavity length is more stable when the device is mounted directly on the optical table (yellow trace) than when it is mounted in the cryostat. The rms cavity length fluctuations integrated from 1 Hz to 100 kHz are $\Delta L_{rms} = 0.29$ pm on the optical table and $\Delta L_{rms} = 1.5$ pm mounted in the cryostat. This decrease in stability can be attributed to mechanical noise entering

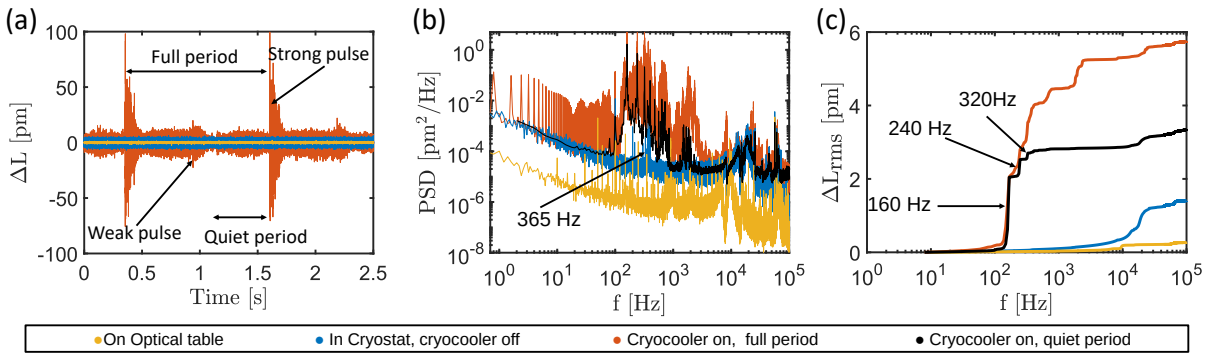

Figure 5.4: Room-temperature stability measurements of the open-cavity device for three different conditions: mounted on the optical table (yellow), mounted in the cryostat under vacuum (blue), and in the cryostat under vacuum and with the cryocooler switched on (red). Note that the measurement in yellow corresponds to an earlier version of the cavity device. (a) Time trace of the signal from the photodiode for a cavity locked at half of the reflection dip. (b) Power spectral density of the signal from the time traces. (c) Cumulative cavity length fluctuation as a function of frequency. The cavity finesse is $F = 1500$ in all cases.

the cavity through the connections of the cryostat to the rest of the lab environment (such as the high-pressure helium flex lines); this noise bypasses the low-pass filter of the optical table. The small peak at 365 Hz in the PSD (blue) in Fig. 5.4(b) corresponds to a mechanical resonance in the base of the cryostat.

Focusing on the measurement with the cryocooler switched on, the time traces show a strong and a weak pulse, both with a period of 1.25 s (0.8 Hz) separated by 0.625 s. In the PSD, we can see the harmonics of this frequency up to kHz frequencies. By calculating the PSD for different bandwidths, we can plot the cumulative cavity length fluctuation in Fig. 5.4(c), which enables the best understanding of the frequencies that contribute most to the mechanical noise.

Because of the large cavity length changes caused by the pulses of the cryocooler, here and in the rest of the paper, we define a quiet period between the weak pulse and the strong pulse, corresponding to 40% of the time between two strong pulses, and we will use it to calculate the PSD and noise characteristics of the cavity device [59, 142]. In this way, the PSD will also be cleaner, as all the cryocooler harmonics caused by the train of pulses in the time trace will be removed, and it will be easier to identify mechanical resonances.

The PSD and the cumulative rms noise are shown as black lines in Figs. 5.4(b) and 5.4(c). During the quiet period, we obtain an rms cavity length fluctuation of $\Delta L_{rms} = 3.4$ pm and 5.7 pm if measured over the full period of the cryocooler. As can be seen from the cumulative cavity length fluctuations, the major contribution to the mechanical noise comes from frequencies lower than 1 kHz, in particular 160, 240, and 320 Hz. These frequencies are not resonances of the cavity device, as they are not visible in the transfer function measurement shown in Fig. 5.3, and they appear in the cryostat measurements only when the cryocooler is switched on. Further evidence of this is presented in Appendix 5.7.1.

5.5 Stability in a closed-cycle cryostat at 4 K

Now we describe the cool-down, realignment, and measurements under cryogenic conditions. With the aid of a copper adapter plate, the open-cavity device is tightly mounted on the base of the closed-cycle cryostat. The cavity is aligned at room temperature using the nanopositioners and the external optics before the system is cooled down to 4 K. By monitoring the free spectral range of the cavity during cool-down, we observe a change in the cavity length of $\Delta L = 5.5$ µm. Once at 4 K, the cavity length can be readjusted with the three piezo motors if needed.

We control the finesse of the cavity by detuning the laser frequency, which changes the mirror reflectivity, such that we obtain the highest finesse cavity that can be locked despite the noise from the cryocooler. The PI parameters of the feedback system are well controlled, as described in Sec. II. In practice, the highest possible finesse is obtained when the peak-to-peak displacement of the cavity length caused by the cryocooler is slightly smaller than the FWHM of the reflection cavity resonance dip; beyond that, the lock is lost during every cryocooler cycle. We usually start with a laser frequency far detuned from the thin-film mirror stop-band center, locking the cavity and optimizing the PI parameters to minimize the mechanical noise in the cavity length, then slightly changing the laser frequency in order to increase the finesse of the cavity, and iterating the procedure until the PI controller is not able to keep the cavity locked.

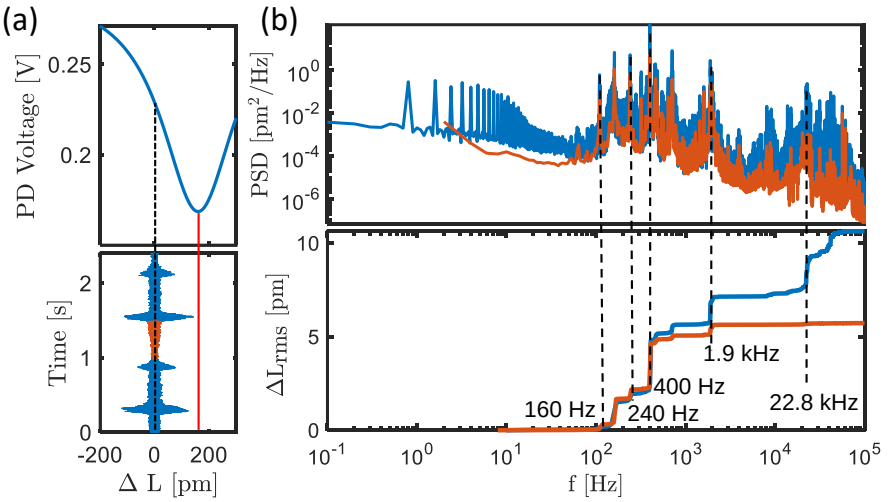

Figure 5.5: Stability measurement at 4 K for a cavity finesse $F = 1800$ ($\lambda = 990$ nm). Panel (a) shows the calibration curve and a section of a time trace of the cavity length displacement. The red-highlighted part in (a) corresponds to the quiet period of the cryocooler. In (b), the PSD and cumulative noise correspond to the quiet period (red) and full period (blue) of the cryocooler. The rms mechanical noise is 5.7 pm in the quiet period and 10.6 pm in the full period.

The thin-film mirror design wavelength is 935 nm, resulting in a cavity finesse of 2500. In our case, the highest finesse we were able to achieve is 1800 at $\lambda = 990$ nm, for which we have a stable lock that lasts for at least 2 days without any adjustment by using the PI parameters $\tau_I = 50\ \mu s$ and $G_P = 0.03$. As described in the previous section, once the cavity is locked at half of the reflection dip, we record ten time traces, each 10 s long, of the photodiode signal. After converting this voltage signal into cavity length fluctuations

(see Appendix 5.7.2), we calculate the PSD and the cumulative integrated rms noise to identify the frequencies that contribute most strongly.

In Fig. 5.5(a), we show a reflection dip and a small portion of the calibrated time trace taken with a locked cavity, which represents the fluctuations of the cavity length from the locked position. The red vertical line corresponds to the maximum peak cavity length fluctuation that allows locking of the cavity, while the red-highlighted part of the time trace corresponds to the quiet period of the cryocooler (40% of the full period). Using the calibrated time trace, we calculate the power spectral density and the cumulative cavity length fluctuation for the quiet period (red) and the full period (blue) of the cryocooler, as shown in Fig. 5.5(b). The total rms mechanical noise in a 100 kHz bandwidth is 5.7 pm during the quiet period of the cryocooler and 10.6 pm during the full period. As it is clearly visible in the plot, also at 4 K, the major contribution to the noise comes from the same low frequencies that were present at room temperature with an operating cryocooler, in particular at 160 and 240 Hz. In addition, now there is also mechanical noise at 400 Hz, which we think is a mechanical resonance of the base of the cryostat that shifted from the room temperature value of 365 Hz.

Only a small part of the noise comes from resonances of the open-cavity device itself, one small contribution at 1.9 kHz (compare Fig. 5.3), and a contribution from 22.8 kHz, which is the oscillation frequency of the feedback loop. We note that the contribution from 22.8 kHz is significant only in the full period curve (blue) because the pulses from the cryocooler bring the feedback close to instability.

5.6 Conclusions and outlook

In conclusion, we have developed an open-access optical microcavity compatible with a tabletop optical closed-cycle cryostat. At 4 K, the open cavity device has stabilities of 5.7 and 10.6 pm rms during the quiet and full periods of the cryocooler cycle, respectively. The device allows for full nanometric but millimeter-range tunability of the cavity along the three spatial directions and two angles and requires only minimal optical realignment when cooling down to 4 K. The key to this is an extremely high-stiffness and compact design, which allows for active feedback stabilization of the cavity with very high bandwidth.

Most importantly, our design does not use a dedicated mechanical low-pass filter, which would complicate the integration of the cavity in a free-space optical setup, essential, for instance, for full polarization control. Nevertheless, a low-pass filter would increase the stability of our open-access optical microcavity. We estimate that a combination of a mechanical low-pass filter at around 50 Hz and electronic filtering in the feedback loop [153,154], will allow us to achieve at cryogenic temperatures the same cavity stability as on an optical table at room temperature.

Finally, we want to point out that for simultaneous locking of the open-access microcavity and operation of, e.g., a cavity-enhanced quantum dot single photon source, the locking laser has to be separated efficiently from the single photons. The micro-mirror array allows us to operate two spatially separate cavities with two different lasers simultaneously; then, one cavity can be used for stabilization and one for quantum dot spectroscopy.

5.7 Appendix

5.7.1 Comparison of cryocooler in low- and high-power mode

The Gifford-McMahon cryocooler used in our cryostat can be operated in low-power (LP) and high-power (HP) modes. We compare here the effects of the two different settings on the stability of the open-cavity device. As a result of the exchange of helium gas undergoing compression-expansion cycles, the cryocooler introduces mechanical noise in the open-cavity device in the form of pulses. The frequency of this cycle is 0.8 Hz for LP and 1.01 Hz for HP mode, corresponding to the frequency at which the compressed gas enters the regenerator through the high-pressure line. In the middle of the cycle, the helium gas expands and returns to the compressor. This results in two mechanical pulses per cycle of the base plate of the cryostat.

In Figs. 5.6(a) and 5.6(b) we show the fluctuation of the cavity length measured over time with the cryocooler in the LP and HP modes, where the cavity length is actively stabilized by locking at half of the reflection dip as explained in the main text. Each plot shows two kinds of pulses corresponding to the high and low pressure parts of the cycle. Comparing Fig. 5.6(b) to Fig. 5.6(a), we see that in addition to the higher frequency of the pulses, the peak-to-peak amplitude of the pulse is also higher as a result of the increased pressure difference of the helium. We calculated the power spectral density

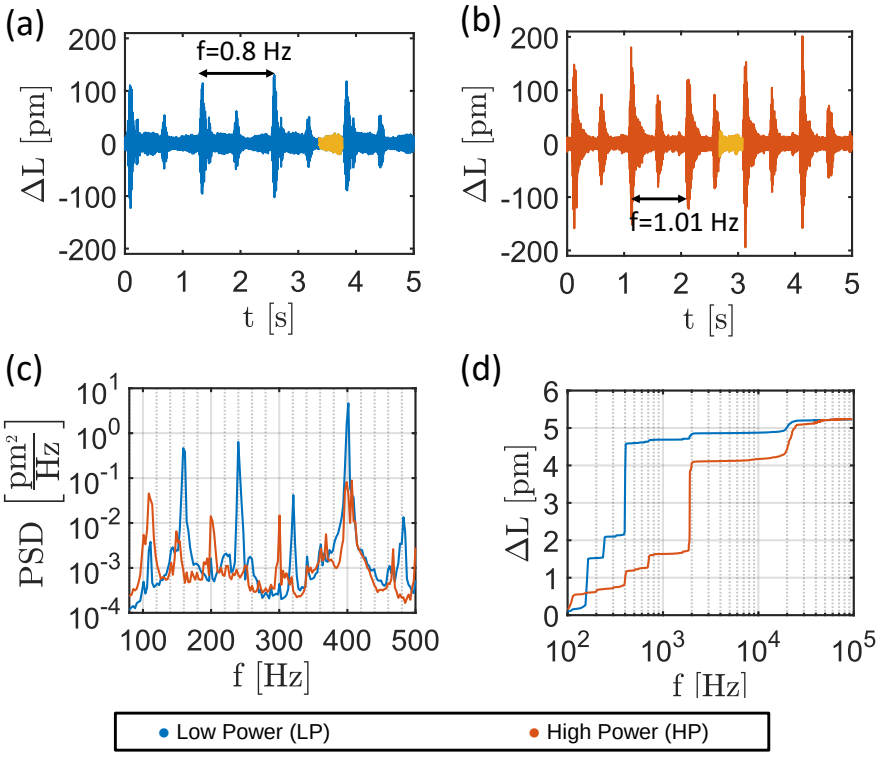

Figure 5.6: Comparison of low- and high-power modes. Panels (a) and (b) show the measured cavity length fluctuations as a function of time for LP (a) and HP (b) modes. The yellow portion of the data are used to calculate the PSD shown in (c) and the cumulative length fluctuations (d), with blue curves for LP and red curves for HP mode.

(PSD) as explained in the main text by considering the yellow sections of the time traces

in Figs. 5.6(a) and 5.6(b) which correspond to the quiet period, i.e. 40% of the cycle for the high power setting. We also considered the same section for the low power mode, so that the frequency separation of the points in the PSD is the same for both configurations, making a comparison easier. As explained in the main text, we take ten time traces of 10 seconds each. For each time trace, we select the yellow sections in each cycle of the cryocooler, calculate the PSD of each section, and finally, average them together. The result of this process is shown in Fig. 5.6(c), where we plot only a small frequency range of 80-500 Hz because outside of this range, there are not many differences between LP and HP modes, except for the peak heights. In particular, in both PSDs, we see a 400 Hz peak corresponding to a resonance of the base of the cryostat, as motivated in the main text. All other low frequency peaks that are visible in the LP mode (160, 240, and 320 Hz) are not present in the HP mode, where there are now three extra peaks at 150, 200, and 300 Hz, most likely harmonics of 50 Hz line noise.

Despite the fact that we do not know the exact origin of the peaks at 160, 240, and 320 Hz, we can conclude that it is the noise introduced by the cryocooler, and these peaks do not correspond to mechanical resonances in the system because otherwise, they should be visible with the cryocooler in HP mode. Because of the constant frequency separation between these peaks, one hypothesis is that they originate from the inverter used in the He compressor, as in LP mode the frequency of the inverter is 40 Hz.

Fig. 5.6(d) shows the cumulative cavity length fluctuation measured in the quiet period of the cryocooler cycle. The total rms noise $\Delta L_{rms} = 5.3$ pm is nearly the same for the two modi, despite the frequencies that contribute to the noise are different. We have used the same PI parameters for both measurements, optimized for the LP mode for minimum vibrations. The feedback loop is less stable in the HP mode due to a higher peak-to-peak amplitude of the pulses excited by the cryocooler, as visible in the 22.8 kHz peak corresponding to the oscillation frequency of the feedback loop.

5.7.2 Calibration of the photodiode signal

In order to measure the stability of the cavity device, we lock the cavity length to half of the reflection dip and record time traces of the voltage signal from the photodiode, as explained in the main text. This voltage must be multiplied by a conversion factor in order to give a measure of the cavity length. While this is trivial in the case of a quiet system where the cavity length does not change much and therefore this conversion factor is simply the slope of the reflection dip at the locking point, in the case of a mechanically noisy system, it is more complicated. In fact, when the cavity length changes significantly, the error signal cannot be approximated anymore as being linear, and in order to retrieve the exact cavity length, we must take the nonlinearities into account.

For this purpose, we calibrate the voltage signal of the photodiode V_{PD} as a function of the cavity length L, by linearly changing the latter via the ring piezo and recording the reflection dip, which is fitted with a Lorentzian,

$$V_{PD} = V_0 + \frac{A}{(L - L_0)^2 + (\frac{w}{2})^2} \ . \tag{5.3}$$

Inverting the equation, we are able to obtain a conversion factor from photodiode voltage to cavity length,

$$L = L_0 \pm \sqrt{\frac{A}{V_{PD} - V_0} - \left(\frac{w}{2}\right)^2} \ , \tag{5.4}$$

where the ± sign is chosen depending on whether the cavity is locked on the left or right side of the reflection dip. A, V_0, L_0 and w are fitting parameters; w is the full width at half maximum of the reflection dip; and L_0 is the resonance cavity length, for which the reflection dip has its minimum.

While this procedure takes into account the nonlinearity of the error function, it still has some drawbacks: for calibration we scan the cavity length at a finite speed, and in the presence of vibrations, the shape of the reflection dip will change depending on the speed at which the cavity is scanned, leading to shifts in the position of the dip, broadening of the cavity reflection dip, and asymmetries. In Fig. 5.7(a), we demonstrate this effect. We have recorded four times a cavity dip, and we observe four very different results, with extracted finesses varying from 1100 to 4600. The real room-temperature finesse is measured to be F = 2500 at a wavelength $\lambda = 935$ nm. A simple way to deal with this is to measure the width of the reflection dip at room temperature without mechanical vibrations as a function of the wavelength of the laser and use this value to obtain the conversion factor of Eq. 5.4, as we expect the reflectivity of the mirrors to be constant from 300 to 4 K.

As an additional proof and to have a better understanding of the phenomena, we show here measurements of the shifts of the resonance widths and dips (w, L_0) and compare them to simulations. For the measurement, we recorded 150 reflection dips at 4 K with

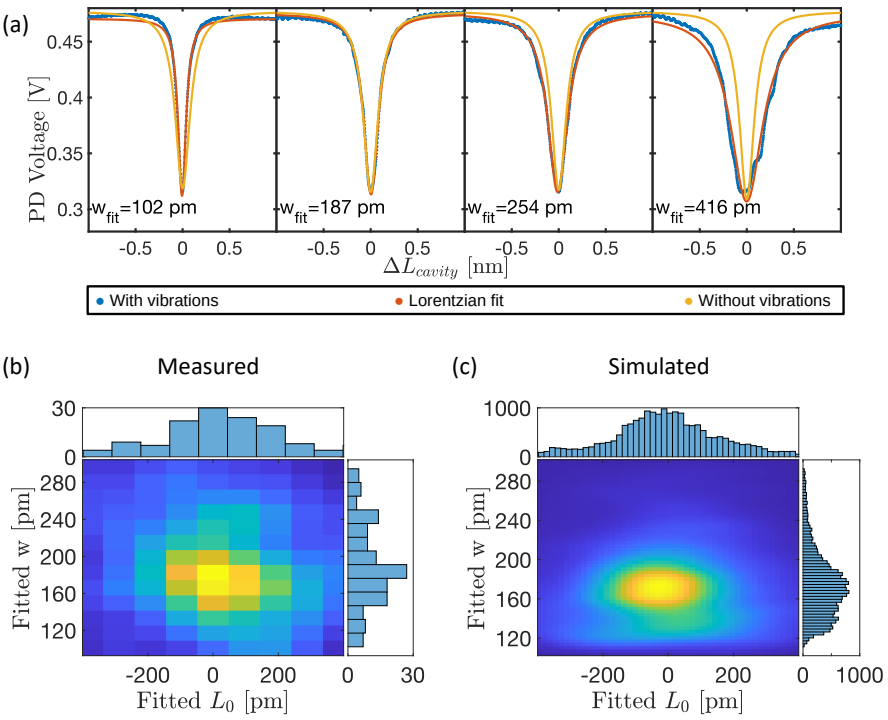

Figure 5.7: (a) In blue, four measurements of a cavity resonance recorded at 4 K with the cryocooler ON, with the same scanning speed but at different times of the cryocooler cycle. In red is the corresponding Lorentzian fit, and in yellow is the real cavity resonance measured at room temperature without vibrations. (b) Scatter plot and relative histograms of the fitted widths and positions of the cavity resonance, measured at 4 K. (c) Scatter plot and relative histograms of the fitted widths and positions of the cavity resonance, the result of a computer simulation.

the mechanical noise generated by the cryocooler by scanning the cavity length repeatedly with the ring piezo. We fit each reflection dip using Eq. 5.3, and we show the resulting scatter plot in Fig. 5.7(b). The data of the scatter plot have been convoluted with a Gaussian mask function with a width of 10 pm to smooth the data due to the low number of samples. The mean value for the width is $w_{mean} = 189$ pm, which is in very good agreement with the real value of 185 pm. The mean value for L_0 is around 0, as we shifted the data manually, since we do not know the real position of the resonance in the absence of vibrations. For the simulation, we used the power reflection coefficient of a Fabry-Perot cavity,

$$R(L) = \left|\frac{E_{reflected}}{E_{incident}}\right|^2 = \left|\frac{r\left(\exp\left(i\frac{4\pi L}{\lambda}\right) - 1\right)}{1 - r^2\exp\left(i\frac{4\pi L}{\lambda}\right)}\right|^2, \tag{5.5}$$

where $L = L_{piezo} + L_{noise}$. $L_{piezo} = v_{piezo} \times t$, and v_{piezo} is the scanning speed of the piezo. For L_{noise} we used the measured displacements from Fig. 5.6 (a) recorded with a cavity locked on the side of the reflection dip, where we compensated for the effect of the integrator: $L_{noise} = (1+I) \times L_{noise}^{lock}$. We chose a mirror reflectivity R $= r^2 = 0.9988$, which correspond to a cavity with a finesse F ~ 2600, and a resonance width of $w \sim 178$ pm at the wavelength $\lambda = 935$ nm. For all other free parameters, such as v_{piezo} and the open loop gain of the integrator I, we have used experimental values.

We have simulated 20000 reflection dips using Eq. 5.5 by randomly shifting in time the experimental L_{noise}, and we fitted the curves with Eq. 5.3 in order to extract w_{fit} and L_0^{fit}. The results are shown in Fig. 5.7(c), where the data have been smoothed by convolution with a Gaussian mask function. The mean values are $w_{mean} = 179$ pm and $L_0^{mean} = -1.7$ pm. Visually, the distribution in Fig. 5.7(c) is clearly shifted toward negative L_0. We hypothesize that this is because of the forces that keep together the two mirrors, i.e., gravity and the three metal springs holding together the top plate and the bottom part of the open cavity device. Since L_0 is the rest-length of the cavity, mechanical vibrations in the open-cavity device will exert sinusoidal forces that act in the same direction as gravity and the spring force for $L_0 < 0$, and in the opposite direction for $L_0 > 0$, causing the asymmetry visible in the histogram. The very good agreement between the measured data and the simulation, as well as the comparison to the reflection dip widths measured in the absence of noise, shows us that indeed we can calibrate the photodiode signal at 4 K with the parameters measured at room temperature for the same wavelength.